Advantage of wavelet technique to highlight the observed geomagnetic perturbations linked to the Chilean Tsunami (2010).

V. Klausner,[1,2,3] Odim Mendes,[1] Margarete O. Domingues,[1] Andres R. R. Papa,[2,4] Robert H. Tyler,[5] Peter Frick,[3] and Esfhan A. Kherani.[1]

Corresponding author: V. Klausner, Space Geophysics Division - DGE/CEA, National Institute for Space Research, Av. dos Astronautas, 1758, Predio Sigma, Sala 41, CEP 12227-010, Sao Jose dos Campos, SP, Brazil. (virginia.oliveira@inpe.br)

[1]National Institute for Space Research, São José dos Campos, SP, Brazil.

[2]Department of Geophysics, National Observatory, Rio de Janeiro, RJ, Brazil.

[3]Laboratory of Physical Hydrodynamics, Institute of Continuous Media Mechanics, Perm, Russia.

[4]State University of Rio de Janeiro, Rio de Janeiro, RJ, Brazil.

[5]Department of Astronomy, University of Maryland, Maryland, College Park, USA.

Abstract. The vertical component (Z) of the geomagnetic field observed by ground-based observatories of the INTERMAGNET network has been used to analyze the induced magnetic fields produced by the movement of a tsunami, electrically conducting sea water through the geomagnetic field. We focus on the survey of minutely-sampled geomagnetic variations induced by the tsunami of 27th February, 2010 at Easter Island (IPM) and Papeete (PPT) observatories. In order to detect the tsunami disturbances in the geomagnetic data, we used wavelet techniques. We have observed a 85% correlation between the Z-component variation and the tide gauge measurements in period range 10 to 30 minutes which may be due to two physical mechanisms: gravity waves and the electric currents in the sea. As an auxiliary tool to verify the disturbed magnetic fields, we used the maximum variance analysis (MVA). At PPT, the analyses show local magnetic variations associated with the tsunami arriving in advance of sea-surface fluctuations by about two hours. The first interpretation of the results suggests that wavelet techniques and MVA can be effectively used to characterize the tsunami contributions to the geomagnetic field and further used to calibrate tsunami models and implemented to real-time analysis for forecast tsunami scenarios.

1. Introduction

Ocean water is electrically conducting and as it flows through the Earth's magnetic field small secondary magnetic fields are generated at the expense of some of the flow's kinetic energy. Aside from being an interesting physical effect, there is currently great interest from a practical perspective because of the potential for using these magnetic fields to remotely sense ocean flows [*Stephenson and Bryan*, 1992; *Tyler et al.*, 1999, 2003; *Manoj et al.*, 2006]. The magnetic fields generated by tsunami flow is a specific example of this effect and is the application considered in this paper.

The geomagnetic field is described as a complicated function of space and time. Ground based magnetic measurements show a repetitive diurnal variation on geomagnetically quiet days. But there is a great variety of irregular variations that occur from time to time that characterizes the "disturbance-time fields". Periods of great disturbance are called, by analogy with the weather, "magnetic storms" [*Parkinson*, 1983].

Some evidence of the influence of oceanic tides on the magnetic daily variation has been obtained by *Larsen and Cox* [1966]. They found small semi-diurnal variations of the Z-component at a coastal site (Cambria, California) and at two island observatories (Honolulu and San Miguel) that could not be explained by the atmospheric tidal theory. They suggested that these variations must be due predominantly to oceanic tides. It is important to mention here that the conductivity of the ocean does not vary significantly with time, unlike the ionospheric conductivity. As a consequence, the seasonal variation of the oceanic contribution is expected to be smaller than the ionospheric contribution [*Cueto et al.*, 2003].

Manoj et al. [2011] searched for the geomagnetic contributions due to the moderate tsunami in the Pacific ocean generated by the 8.8 Chilean earthquake (2010) at three different magnetic observatories (Papeete (PPT), Huancayo (HUA) and Easter Island (IPM)). In their investigation, only IPM magnetograms presented a variation of 1 nT in the vertical component of the magnetic field (Z) during the time of the tsunami propagation. Also, *Utada et al.* [2011] observed a periodic fluctuation at CBI observatory (on Chichi-jima Island) starting from around 7:00 UT due to the arrival of the Japanese tsunami on 11th of March, 2011. Considering quiet conditions, *Tyler et al.* [1999] discussed that the major difficulty to determine the magnetic ocean generated signals are the weak values compared to the signals from other sources.

In a short description, the induced magnetic field generated by the ocean can be classified by two components: toroidal and poloidal. The toroidal component is generated by the electrical currents closing in the vertical plane and can reach up to 100 nT but is confined to the ocean and the upper crust. The poloidal component is much weaker, between 1 and 10 nT, and arises from the electrical currents closing in the horizontal plane, however it reaches outside of the ocean to remote lands and satellite locations [see *Tyler et al.*, 2003; *Manoj et al.*, 2006, and references therein].

A theoretical description of the magnetic fields generated by tsunami flow was discussed by *Tyler* [2005]. In this work, *Tyler* [2005] employed a simple relationship between the tsunami generated magnetic field and the sea-surface displacement using the long-wavelength assumption.

Another mechanism of the geomagnetic field induction is propagation of acoustic gravity waves due to tsunamis. *Iyemori et al.* [2005] observed long period Pc5 pulsations with a period of approximately 3.6 minutes and 9 minutes during the Sumatra tsunami and also, they speculated about short period pulsation Pc3 (about 30 seconds) as a result of magnetic field line resonance with a magnetosonic wave generated from the electric and magnetic fields of the dynamo current caused by the Earthquake. According to *Iyemori et al.* [2005], these pulsations were generated by the dynamo action in the lower ionosphere set up by an atmospheric pressure pulse which propagated as an acoustic wave when the ocean floor suddenly moved vertically. Also, *Artru et al.* [2005] detected gravity waves with period range 10 to 30 minutes which propagate horizontally at approximately the same speed as the tsunami observed in Peru on 2001, June, 23. As mentioned by *Artru et al.* [2005] the tsunami waves are expected to couple with atmospheric gravity wave due to the tsunami long wavelengths.

The mechanism of the acoustic and gravity-acoustic waves for generation of geomagnetic variations consists of the vertical wind oscillation caused by the duct resonance set up by the earthquake, a wide area at the epicenter suddenly lifted up or depressed and an atmospheric pressure variation propagates upward as acoustic and gravity-acoustic waves. These waves generate a electric field by polarization and by the dynamo current in an east-west direction over the epicenter. The polarized electric field is mapped along the geomagnetic field to the ionosphere. The electric field then generates the ionospheric currents in both east-west and north-south direction by Pedersen and Hall ionospheric conductivities causing geomagnetic oscillations on the ground [see *Iyemori et al.*, 2005, and references therein].

For the Japan tsunami (2011), *Kherani et al.* [2012] have presented the detailed travel-time diagram (TTD) of the magnetic field disturbances using a chain of magnetometer stations. They have also presented a simulation of these disturbances based on the tsunami-atmosphere-ionosphere (TAI) coupling mechanism, which was presented theoretically for the first time by *Peltier and Hines* [1976] using an analitical approach based on isothermal atmosphere hypothesis. Later, *Lognonné et al.* [1998] presented an additional theoretical validation of TAI with a normal mode sommation theory for a planet with elastic ocean and viscous atmosphere. Finally, the TAI was theoretically discussed again by *Occhipinti et al.* [2006] using a 3D pseudo-spectal propagator with an adiabatic and non-isothermal atmosphere; additionally *Occhipinti et al.* [2006] introduce also the ionosphere, and supported the theoretical modeling with total electron content observations by altimeters. More details and references about the tsunami and earthquake detection by ionospheric sounding, as well as the coupling mechanism can be found in *Occhipinti et al.* [2013].

In the TAI mechanism, Acoustic-Gravity-Waves (AGWs) are excited by the tsunami which then drive the currents in the ionosphere and gives rise to the magnetic field disturbances. *Kherani et al.* [2012] have presented a detailed synthetic TTD of the magnetic field disturbances and found fairly good agreement with the observed TTD. By considering the full spectrum of the dissipative AGWs, an early development (within 10 minutes from the tsunami initiation) of magnetic field and total-electron-content (TEC) disturbances in the ionosphere, were explained which otherwise could not be explained solely by the slowly propagating gravity waves. In their work, most of the dominant wave features such as the early arriving acoustic and late arriving gravity waves were identified in both observed and synthetic TTDs which affirms that the complete dissipative AGWs, rather than the pure gravity waves, should be considered in a TAI coupling mechanism.

In this work, we focused on the survey of geomagnetic variations induced by the tsunami of 27th February, 2010. Wavelet transforms proved to be a useful tool in atmospheric signal analysis [see *Domingues et al.*, 2005, and references therein]. The gapped wavelet transform and discrete wavelet technique has been applied in order to detect the disturbed magnetic fields in the geomagnetic data as used in *Mendes et al.* [2005]; *Mendes da Costa et al.* [2011]; *Klausner et al.* [2013]. Thus, this work aims to evaluate the use of the wavelet techniques as a way to identify the magnetic contributions related to tsunamis on the geomagnetic field components, particularly in the Z-component. Also, we use the maximum variance analysis (MVA) to verify the results and the disturbed magnetic fields detected by the wavelet technique that may be associated with the tsunami propagation.

The outline of this paper is as follows: Section 2, Dataset, ground magnetic measurements set; Section 3, the applied methodology; Section 4, the results achieved by the analysis; and Section 5, the conclusions of our work.

2. Dataset

In this section, we first describe the data used to study the geomagnetic variations due to the tsunami-generated magnetic fields. The tsunami event of 27th of February, 2010 is presented. For this event, we have chosen two ground magnetic measurements. We have also selected the tide-gauge measurements at or nearby the chosen magnetic observatories.

We selected magnetic observatories belonging to the INTERMAGNET program (http://www.intermagnet.org) that were influenced or more directly affected by the tsunami. By international agreement, there are two usual systems that can represent the Earth's magnetic field: the XYZ and the HDZ system [see *Campbell*, 1997, and references therein]. The X, Y and Z stand for northward, eastward and vertical into the

Earth directions, the H, D and Z stand for horizontal component, declination (angular direction of the horizontal component related to the geographical north) and vertical (into the Earth). The H-component is more affected by the solar-magnetospheric interactions, consequently, also the X- and Y-component. These variations, specially those associated with the ring current, are a major contribution to the magnetograms at observatories located at low and mid-latitude regions. Because the Z-component is less affected than the H-component at the low latitudes of the observatories selected, we decided to use the Z-component to detect the geomagnetic variations induced by the tsunami.

Regarding geomagnetic conditions, the 27 February, 2010 corresponded to a very quiet day. The Dst index presented the minimum of $-2\,\mathrm{nT}$ and the maximum of $4\,\mathrm{nT}$ and the SYM-H index presented the minimum of $-9\,\mathrm{nT}$ and the maximum of $5\,\mathrm{nT}$, both of which show smooth variations (see Fig. 1). When the magnetosphere is under quiet conditions the behavior of the recorded Z-component should be much smoother than its behavior in the disturbed periods, making easy the identification of the variations induced by the propagation of the tsunami. The SYM-H index is essentially the same as the traditional hourly Dst index. The main characteristic of the 1 minute time resolution SYM-H index is that the solar wind dynamic pressure variation is more clearly seen than through indices with lower time resolution. Its calculation is based on magnetic data provided by eleven observatories of low and medium latitudes. Only six of these eleven observatories are used for its calculation of each month, some observatories can be replaced by others depending on data conditions.

Near the coast of central Chile, on the 27 th of February, 2010 at 06:34 UT occurred an earthquake with magnitude 8.8 M_w. The epicenter was located on Lat. $-36.1°$ and

Long. $-72.6°$ at 55km depth. As reported by *Pararas -Carayannis* [2010], shortly after the earthquake, tsunami waves hit the coastal area of the Central Chile. The tsunami overtook the coastal cities as Talcahuano, Coquimbo, Antofasta and Caldera, as well as the Juan Fernández Islands. The NOAA Pacific Warning Center released a bulletin of number 018 and a tsunami warning was issued at 00:12 UT on 28 February, 2010 for a large number of islands and countries in (or near) the Pacific basin.

In the region of Callao La Punta, Peru, the observed and computed tsunami time arrival were coincident, both at 10 : 34 UT with amplitude of up to 0.69 m. We used the sea level measured at this region as a guide to the arrival tsunami at IPM (see Fig. 2). For PPT, the observed tsunami initial arrival time was at 17:33 UT and the computed time was at 17:47 UT with amplitude up to 0.22m (see Fig. 3).

In this work, the magnetic observatories considered for this event were: Easter Island (IPM) and Papeete (PPT), with the geographic and geomagnetic coordinates presented in Table 1. Fig. 4 display the localization of tide gauge and magnetic stations with their respectively IAGA codes. We selected the same two observatories used by *Manoj et al.* [2011] to study the geomagnetic contributions due to the Chilean tsunami (2010) and excluded the observatory of HUA located in Peru due to the equatorial electrojet effects. In their study, only the IPM observatory showed a periodic variation of 1 nT in the vertical component (Z) caused by the tsunami started at 11:35 UT, and the other two observatories did not show concurrent variations.

3. Methodology

We apply in this work both continuous and discrete wavelet transform. For the continuous, we used the Gapped wavelet technique introduced by *Frick et al.* [1997] due to its property of dealing with gaps and the algorithm of Discrete Wavelet Transform (DWT) described by *Mendes et al.* [2005]. We detected there the disturbed transients on the H (or X) component of the magnetic field due to geomagnetic storms. Here, we use a similar technique during a geomagnetically quiet period in the Z component of the magnetic field to characterize the magnetic variations supposed to be produced by the propagation of tsunamis. However, we used as an auxiliary tool, the maximum variance analysis (MVA), to be sure that these variations are really associate with the tsunamis. The MVA is able to verify the changes in the direction of the magnetic field due to the poloidal component of the induced magnetic field generated by the ocean due to the tsunami water displacements.

3.1. Gapped Wavelet Analysis

In this work, we applied the gapped wavelet technique which was first introduced by *Frick et al.* [1997] and afterwards improved in *Frick et al.* [1998]. The leading idea of the gapped technique is to restore the admissibility condition which is broken when applied on data gaps.

Following *Frick et al.* [1997], we separate the analyzing wavelet in two parts, the oscillatory part $h(t)$ and the envelope $\varphi(t)$,

$$\psi(t) = h(t)\,\varphi(t), \tag{1}$$

$$h(t) = \exp(i\,\omega_0\,t), \tag{2}$$

$$\varphi(t) = \exp\left(\frac{-t^2}{2}\right). \tag{3}$$

When the wavelet is disturbed by the gap, we can restore the admissibility condition by including a function $\mathsf{K}(\mathsf{a}, \mathsf{b})$ in the oscillatory part of the wavelet,

$$\widetilde{\psi}(t, b, a) = \left[h\left(\frac{t-b}{a}\right) - \mathsf{K}(a, b)\right] \varphi\left(\frac{t-b}{a}\right) \tag{4}$$

and requiring,

$$\int \widetilde{\psi}(t)\, dt = 0 \tag{5}$$

The introduced function $\mathsf{K}(a, b)$ can be determined for each scale a and position b from (4) and (5).

It was shown that this technique not only suppresses the noise caused by the gaps and boundaries, but improves the accuracy of frequency determination of short or strongly gapped signals [*Frick et al.*, 1998].

3.1.1. Wavelet Cross-correlation Analysis

The approach of this work is to use the wavelet cross-correlation to study the correlation between a pair of datasets from different locations as a function of scale (see *Nesme-Ribes et al.* [1995] and *Frick et al.* [2001] for more mathematical details):

$$\mathcal{C}(a) = \frac{\int \mathcal{W}_1(a, t)\, \mathcal{W}_2^*(a, t)\, dt}{\left(\int \mathcal{W}_1(a, t)^2\, dt\, \int \mathcal{W}_2(a, t)^2\, dt\right)^{\frac{1}{2}}} \tag{6}$$

where $\mathcal{W}_i(a, t) = |W_i(a, t)| - \overline{|W_i(a, t)|}$, W_i are the wavelet coefficients and $\overline{W_i}$ is the arithmetic mean in time for $i = 1$ or 2.

The wavelet cross-correlation allows us to check the interaction between two sets of data for each considered scale. In order to determine the dominating periods, we choose the scales where the correlation has the maximum value in the geomagnetic correlation spectrum.

3.2. Discrete Wavelet Transform (DWT) methodology

The discrete wavelet transform (DWT) is a multi-level linear transform based on a multirresolution analysis construction [*Daubechies*, 1992]. This analysis produces the so-called wavelet coefficients at different levels and it is proved that their amplitudes can be used to study the local regularity of the analyzed data [*Mallat*, 1999]. If the wavelet coefficient amplitude is very small, it means that more regular is the analyzed data. Therefore, where the amplitudes are large we can associate it to some disturbance on the signal [*Mendes et al.*, 2005].

The wavelet transform in level $j+1$ is given by

$$d_k^{j+1} = 2\sum_m g(m-2k)\, c_m^j, \tag{7}$$

where g is a high-pass filter, d_k^{j+1} is the wavelet coefficient at level $j+1$, and c_m^j are the scale coefficients at level j. In this transform,

$$c_k^{j+1} = 2\sum_m h(m-2k)\, c_m^j, \tag{8}$$

and h is a low-pass filter.

In this study, we considered $j=0$ as the most refined level of the multi-level decomposition which is associated with one minute data resolution. In other words, $c_k^{j=0}$ is the mean time fluctuation computed from the raw magnetogram data.

We choose the Haar wavelet, therefore the non-zero filter values are $h = [\frac{1}{2}, \frac{1}{2}]$ and $g = [\frac{1}{2}, -\frac{1}{2}]$. This choice is based on the property of this wavelet to reproduce constant functions locally, this means that it is very sensitive to local variations. This property is the key point of this study of local regularity. Choosing the order of the analyzed wavelet you decide the local polynomial approximation, consequently, with the choice of Daubechies wavelet of order 1, we focus our study in local constant polynomial approximation. Therefore, the amplitude of the wavelet coefficient are related to the local approximation error [*Mallat*, 1991].

With the choice of Haar wavelet and sampling rate of one minute, the first three multi-levels are associated with pseudo-periods (central-periods) of 2, 4, and 8 minutes. On the physical point of view, these periods are related to the tsunami wave arrival and the sea water displacements.

3.3. Maximum variance analysis

We used the maximum variance analysis (MVA) to verify the identification done by the discrete wavelet technique, as an alternative way to analyze the influence of the tsunami on the geomagnetic field. The maximum variance analysis (MVA), in the case of this work, uses a set of magnetic field components to determine the direction to minimize the standard deviation of the magnetic field component in that direction. MVA has been applied to magnetometer data to define a new set of vectors relative to some natural boundary such as the magnetopause or the bow shock [*Sonnerup and Cahill*, 1967; *Sonnerup*, 1976]. In that context, the main purpose of MVA was to find an estimate of the orientation of a nearly one-dimensional discontinuity such as current sheet or wave front.

The boundary normal coordinates system (LMN system) is defined as having its M-direction along the direction with minimum variance in the magnetic field, its L-direction along the medium variance and its N-direction along maximum variance, see *Russell and*

Elphic [1978] for more details. In our case, the M-direction is along the direction of the electrical current on the horizontal sea sheet, the L-direction and N-direction are along the tsunami velocity propagation perpendicular to the geomagnetic field line and along the vertical sea sheet.

It is the custom to construct a curve in this new space defined by the MVA vectors in two projections called magnetic hodograms. A tutorial on the main properties and applications of the MVA can be found, for instance, in *Paschmann and Daly* [1998].

4. Results and analysis

In this section, we present first the results concerning the wavelet techniques and after those concerning MVA.

4.1. Results using GWT

In order to detect the same geomagnetic tsunami contributions observed by *Manoj et al.* [2011], we applied the continuous gapped wavelet transform (GWT) on IPM magnetograms. One of the reasons for using GWT is that the geomagnetic data can include gaps up to one minute length. Fig. 5 shows the geomagnetic behavior for the days 26 to 28th of February, 2010 using GWT. The GWT can be used in the analysis of geomagnetic signal to obtain information on the frequency or scale variations about ionospheric and/or magnetosppheric phenomena due to its properties of detecting the localization of these structures in time and/or in space [see *Klausner et al.*, 2013, for more details]. It is possible to analyze a signal in a time-scale plane, the so called wavelet scalogram. In analogy with the Fourier analysis, the square modulus of the wavelet coefficient, $|W(a,b)|^2$, is used to provide the energy distribution in the time-scale plane. Each panel shows: a) the Z-component (top) and b) the wavelet square modulus (bottom). In the scalogram, areas of stronger wavelet power are shown in dark red on a plot of time (horizontally) and period time scale (vertically). The areas of low wavelet power are shown in dark blue.

Before applying the GWT to the magnetograms, we removed the daily variations from the data. We calculated the smooth average from 30 days of quiet day daily variations using days belonging to the same season in order to prevent the ionospheric dynamo seasonal changes. Also, we eliminate a Gaussian white noise from the data, since it is the simplest to be modeled. The signal was estimated by isolating the coherent structures which have a high correlation with the signal components of the wanted data. The method of extraction of coherent structures consists in using a wavelet basis which approximates piecewise smooth functions efficiently but does not correlate well with high frequencies oscillations. It is inspired by a theorem of Donoho which states that the way to denoise a signal f, sampled on N points and perturbed by an additive Gaussian noise of variance σ^2, is to take its discrete wavelet transform. The method selects only those wavelet coefficients with absolute value larger than the threshold $\epsilon = (2\sigma^2 log(N))^{\frac{1}{2}}$ and sets all the other coefficients to zero. After that, the signal is reconstructed with the remaining wavelet coefficients (see *Farge et al.* [1999] for more details). For the estimation of these coherent structures we use some packages from the free software WaveLab (available on-line in the URL http://www-stat.stanford.edu/ wavelab/) to filter the data.

On the 27th February, 2010, the scalogram shows a strongest wavelet power area from, approximately, 11:00 UT to 14:00 UT. The physical phenomena responsible for wavelet power area appear to have period of a few minutes, mainly from 8 to 16 minutes. The same period range of geomagnetic pulsations were detected by *Iyemori et al.* [2005] due to tsunami related gravity wave. For the Japan tsunami, 5-10 minutes geomagnetic pulsations were detected by *Kherani et al.* [2012], and these pulsations were shown to be associated with the gravity waves. The presence of periodicities $\sim$ 8 minutes was explained on the basis of mesospheric ducting of the gravity waves which is the region of the atmosphere around 90-110 km altitude that oscillates with the Brunt-Vaisala frequency $\sim$ 8 minutes. The presence of this period in Fig. 5 which can only be associated with the mesospheric duct, suggests that the magnetic field perturbations detected in Fig. 5 are partly caused by the ionospheric currents driven by the gravity waves Moreover, *Kherani et al.* [2012] have found the early arrival of unducted large vertical wavelength gravity waves followed by the late arrival of the ducted short-wavelength gravity waves into the ionosphere. In this context, Fig. 5 shows the development of ducted (with period $\sim$ 8 minutes) disturbances later than the unducted (period >15 minutes) disturbances. This feature is consistent with the mechanism discussed by *Kherani et al.* [2012] and thus it may be said that the magnetic disturbances presented in Fig. 5 are partly arising from the TAI coupling mechanism.

On the scalograms of the day of 26th February, 2010, these pulsations were not detected. On the day of 28th February, 2010, these pulsations were detected between 05:00 to 09:00 UT. However, these pulsations were also detected at the same day at the same time on the PPT scalogram (see Fig. 6) showing that the physical phenomena responsible for these pulsations affected the magnetosphere globally and it was not a local phenomena as the tsunami.

The pulsations due to the propagation of the gravity wave generated by the tsunami was also detected on PPT magnetograms (Fig. 6). Period range between 10 and 30 minutes were detected between 16:00 and 21:00 UT on the PPT scalogram. Around this time the ionosphere was the quietest and the SYM-H geomagnetic index did not indicate any magnetic storm or unusual solar activity. However, at PPT the daily ionospheric variations start about 16:00 UT and the ionospheric dynamo (Sq) starts around this time but we filtered the daily variations from the data. In order to eliminate any doubts from tsunami-induced magnetic fields due to the propagation of the acoustic wave around 16:00 UT, we applied GWT on the PPT tide gauge dataset and after we analyzed the wavelet correlation between the PPT magnetogram and PPT tide gauge dataset.

On Fig. 7, the tsunami waves were detected on the scalogram with period range between 10 and 30 minutes from 18:00 to 22:00 UT. Comparing Fig. 6 to Fig. 7, the square modulus of the wavelet coefficients with stronger power than the background in period range between 10 and 30 minutes were detected about two hours in advance.

As mentioned by *Artru et al.* [2005],the typical tsunami wave period range is approximately the same period as the tsunami related gravity wave. In this case, we applied wavelet cross-correlation to check the interaction between these two waves for period range between 10 and 30 minutes.

During the tsunami propagation, the correlation coefficient has a value up to 0.85 for the wave period range between 10 and 30 minutes (see Fig. 8). In contrast, the correlation coefficient value remains below 0.54 in a period previous the tsunami arrival.

4.2. Results using DWT

Fig. 9 shows the wavelet signatures for the three first decomposition levels. Panels (a) to (b) correspond to magnetic observatories of IPM and PPT, respectively. In each panel, from top to bottom are displayed the magnetogram (Z-component), and the $dj = (d^j)^2$ for $j = 1, 2, 3$ wavelet decomposition levels.

The NOAA Pacific Warning Center predicted the tsunami time arrival at 12:05 UT for the Easter Island, IPM. In Fig. 9(a), the first decomposition level presented a main structure of coefficients between 11:58 UT and 13:24 UT and a secondary spike at 15:36 UT. Also, it presented a sequence of small structures between 16:54 UT and 24:00 UT. The $(d^j)^2(j = 2)$ showed the highest coefficients at 12:28 UT and 12:40 UT and $(d^j)^2(j = 3)$ at 12:00 UT. On the other hand, $(d^j)^2(j = 2, 3)$ presented less structured features than $(d^j)^2(j = 1)$. In $(d^j)^2(j = 3)$ it was possible to notice four peaks, one at 12:00 UT, a second one at 12:15 UT, a third one at 12:32 UT and the last at 13:35 UT, followed by two main structure of coefficients between 14:30 UT and 16:30 UT and between 20:30 UT and 22:30 UT. These wavelet coefficients with higher amplitudes than the background ones determine the time interval candidates of the magnetic contribution to the tsunami propagation.

In Fig. 9(b), the main wavelet coefficient structures are restricted to the period between 15:36 UT and 21:52 UT. The $(d^j)^2(j = 1, 2, 3)$ presented surprisingly similar wavelet signatures. These wavelet coefficients might be associated with the abrupt variations on the magnetic field associated with the tsunami activity. The tsunami-induced electromagnetic candidates were detected about two hours in advance.

The DWT can improve the hard task of visual inspection developed by *Manoj et al.* [2011] and *Utada et al.* [2011]. The proposed technique has also the advantage to detect objectively local variations on the analyzing data.

The same analysis shown on Section 4 was performed on the day before and on the day after the tsunami arrival using PPT observatory for comparison purposes. Fig. 10 shows the magnetogram (Z component) and the $dj = (d^j)^2$ for $j = 1, 2, 3$ decomposition levels for PPT the day before, (a) 26th February, 2010, and the day after, (b) 28th February, 2010.

The 26th February, 2010 was a geomagnetically quiet day, Fig. 10(a). The SYM-H index presented the minimum of $-16\,$nT and the maximum of $-3\,$nT with very smooth variations, similar to the 27th February, 2010, see Fig. 1. It is possible to notice that the wavelet coefficients with high amplitudes only appears between 19:00 to 21:00 UT. The reason is that, when the magnetosphere is under quiet conditions, the geomagnetic signal can be considered as smooth, and therefore, the local approximation of the wavelet analyzing function is good and, consequently, the wavelet coefficients which are the local errors of this approximations are negligible. However, the increase of the wavelet coefficient amplitudes between 19:00 to 21:00 UT might be explained by the passage of the solar terminator (ST) which causes the generation of gravity waves, turbulence and instabilities in the ionosphere plasma. As discussed by *Afraimovich* [2008], the ST passage generates wave processes in the ionosphere which have duration of about 1–2 hours and a time shift of about 1.5–2.5 hours after the ST appearance.

On the other hand, on 28th February, 2010, Fig. 10(b), the SYM-H index presented the minimum of $0\,$nT and the maximum of $16\,$nT, see Fig. 1. Usually the positive variations on the Dst index, consequently on the SYM-H index, are mostly caused by magnetospheric compressions due to interplanetary shocks. As mentioned by *Karinen and Mursula* [2005], it often corresponds to the initial phase of geomagnetic storms. The wavelet coefficients amplitude is associated with abrupt signal variations. In this case, the highest amplitudes of the wavelet coefficients indicate the disturbed magnetic fields due to a development of a geomagnetic storm. The wavelet coefficient structures appear between 06:00 UT and 08:00 UT, 12:00 UT and 14:00 UT, 16:00 UT and 20:00 UT and 22:00 and 24:00 UT at the three decomposition levels. This coefficients are related to these positive variations on the Dst index.

In this work, we were able to distinguish the magnetic variations induced by the tsunami from geomagnetic activity because the 27th February, 2010 was a geomagnetically quiet day. During geomagnetic storms, it is difficult to connect the observed perturbations to the tsunami propagation, due to the dynamic variations produced by magnetospheric activity. However, Z-component monitoring could potentially be used in concert with ionospheric measurements [*Occhipinti et al.*, 2006, 2011, 2013; *Rolland et al.*, 2010; *Kherani et al.*, 2012] and applied in a future tsunami early warning system.

4.3. Results using MVA

Fig. 11 and Fig. 12 show the time series of the filtered geomagnetic field measurement (Z-component) and its transformation to boundary normal coordinates (LMN), respectively, both for the IPM event. We applied MVA on the wavelet filtered data because it allows us to analyze the LMN relations on a given range of scales. The hodogram was made using a cycle of the sinusoidal signal (peak to peak) measured on the Z-component from 11:00 UT until 14:00 UT, as shown in Fig. 11. The peaks were measured at the following time intervals of 12:20 UT – 12:31 UT and 12:31 UT – 12:42 UT.

Fig. 12 presents the hodogram obtained from the analysis of Fig. 11. It shows a polarized magnetic field variation induced by tsunami wave in the boundary normal components. In the plane of maximum variance, we can notice a signature of polarized magnetic field that occurs during the time of tsunami propagation which might be due to the electric currents induced in the sea. This polarized magnetic field has approximately the variation of 0.5 nT which corresponds to the magnitude order expected from tsunamis disturbances.

As *Utada et al.* [2011] calculated in their work, we also applied the Biot-Savart law (ignoring the electromagnetic induction) to calculate the induced magnetic fields by the tsunami wave propagation. Considering the distance between the site and the source current of 100 km, the tsunami height of 0.5 m, the tsunami wavelength of 100 km, the propagating velocity of the tsunami 220 m/s, and the vertical geomagnetic component at IPM of $19,000\,\mathrm{nT}$, the intensity of the induced magnetic field field is estimated to be as large as $1.4\,\mathrm{nT}$.

The same analysis was done for the data from the magnetic observatory of PPT. Fig. 13 shows the time series of filtered Z-component and Fig. 14 shows its transformation to boundary normal coordinates (LMN) for PPT observatory using the day of the tsunami arrival at Papeete. Once more, the hodogram was made using a cycle of the sinusoidal signal (peak to peak) measured on the Z-component due to the tsunami propagation, shown in Fig. 13.

Fig. 14 is very similar to Fig. 12. The graphics corresponding to the peak time interval of 18:23 UT – 18:38 UT and 18:38 UT – 19:03 UT. Here, the maximum variance plane also shows a signature of polarized magnetic field presenting approximately the variation of $\pm\,0.5\,\mathrm{nT}$.

5. Conclusions

In this study, we have examined the Chilean tsunami, 2010, using an improved analysis methodology based on wavelet techniques and MVA applied to the Z-component of magnetogram data when no geomagnetic storms were present. We select the IPM and PPT magnetic observatories to determine the magnetic contribution of the tsunami wave propagation through the geomagnetic field.

Our results showed oscillations with a period range from 10 to 30 minutes which can be associated with gravity wave propagation induced by tsunamis. In these conditions, after removing the daily variations from the data, we observe that: (1) the gravity waves observed at PPT has the same period range of the tsunami waves and (2) the ionosphere was very quiet before the tsunami arrival.

Also, at PPT the Z-component variation and the tide gauge measurements showed a maximum of correlation above 85% between 22 to 30 minutes. In this work, we showed a very good correlation between the Z-component variation and the tide gauge measurements in period range from 10 to 30 minutes, and this correlation may be due to two physical mechanisms which are the gravity waves and the electric currents in the sea.

In response to the Chilean tsunami, 2010, the DWT results show that the increase of wavelet coefficient amplitudes associated with the Z-component observed at IPM are well correlated with the arrival of the tsunami waves. A similar increase in the wavelet coefficient amplitudes was also detected at PPT, where a signal was not apparent in the previous analysis using simpler inspection methods. These wavelet amplitudes at PPT appear, however, with about a two-hour lead over the arrival of the sea-surface displacements. A lead of this amplitude is expected because of the closure of electric currents in the sea [*Tyler* , 2005]. The tsunami flow, through motional induction, excites electric currents along the axis of the crests/troughs of the wave (i.e. perpendicular to the tsunami wave fronts). But the current density induced is uniform along the direction of electric current flow only in highly idealized situations (e.g. cylindrical symmetry of all sources and parameters). More generally, there will be convergences/divergences in this directly induced component of the electric current. Because of this, to conserve electric charge there will also be electric currents that close along paths including extensions through the water ahead of the wave. The length scale for this forward closure of electric current may involve all scales over which the flow, main magnetic field, and ocean-layer conductance vary. Additionally, one expects a higher concentration of this forward electric current (and the associated magnetic fields) when the curvature of the wave crest/trough is positive toward the direction of propagation. Inspection of the animated tsunami simulation calculated with MOST forecast model (provided on-line by the NOAA Center for Tsunami Research) shows that at IPM, the tsunami crests/troughs are negative toward the direction of propagation (i.e. there is a concentric wave form propagating away from the source). But by the distant location of PPT, one sees that the wave form has changed and the crests/troughs arrive at this location with positive curvature over a scale of roughly 2000 km.

It is then expected that while the leading electric currents (and associated magnetic signals) may be negligible at IPM, they may be significant at PPT. An observed two-hour lead at PPT corresponds to a forward leading distance of roughly 1600 km when one assumes a propagation speed of 220 m/s (this is obtained from the wave speed $(gH)^{1/2}$, where g is the gravitational acceleration and $H \approx 5$ km is taken to be the average water depth). A realistic simulation of the hydrodynamics and electrodynamic elements of the tsunami are required for clear demonstration of this leading effect (i.e. that the tsunami flow generated magnetic signals at PPT arrive two hours earlier than their flow sources.) But the fact that the two-hour lead corresponds with a leading distance of 1600 km, and that this distance is similar to the 2000 km length scale of the wave curvature seen in the simulated tsunami provides an adequate provisional explanation. Indeed, as stated above, in all but highly idealized geometries one should expect return electric currents cast through the water ahead of the tsunami front, and the maximum length scales for this closure increase as the tsunami wave broadens in time. But note that the density of the electric current involved decreases as the length scale for these return currents increase.

Changes on the geomagnetic field due to a presence of a polarized magnetic field were observed during the tsunami propagation at IPM and PPT and it was estimated to be of amplitude 0.5 nT which is consistent with theoretical expectations. The signature of polarized magnetic field corresponds to the poloidal component of the induced magnetic field generated by the tsunami wave.

Our methodology could be used in a semi-automatic way to characterize the tsunami induced magnetic field. Previous studies of *Manoj et al.* [2011] and *Utada et al.* [2011], employed mainly visual inspection. An automatic detection and classification of tsunami-genic magnetic signals may also be useful to the understanding of the physical processes involved in the tsunami propagation and could be implemented to real-time analysis for forecast scenarios.

Acknowledgments. V. Klausner wishes to thanks CAPES for the financial support of her PhD (CAPES – grants 465/2008) and her Postdoctoral research (FAPESP – grants

2011/20588-7 and 2013/06029-0). The authors would like to thank the NOAA and the INTERMAGNET program for the datasets used in this work, V. Menconi (FAPESP 208/09736-1, CNPq 312486/2012-0 and 455097/2013-5) for his helpful computational assistance and the comments by G. Occhipinti and anonymous referee which led to improvement of this paper.

References

Afraimovich, E. L. (2008), First GPS-TEC evidence for the wave structure excited by the solar terminator *Earth, Planets and Space*, *60*, 895–900.

Artru, J., V. Ducic, H. Kanamori, P. Lognonné and M. Murakami (2005), Ionospheric detection of gravity waves induced by tsunamis, *Geophysical Journal International*, *160*(3), 840–848.

Campbell, W. H. (1997), Introduction to Geomagnetic Fields, *Cambridge University Press*, *New York*.

Cueto, M., D. McKnight, and M. Herraiz (2003), Daily geomagnetic variations on the Iberian peninsula, *Geophysical Journal International*, *152*(1), 113–123.

Daubechies, I. (1992), Ten lectures on wavelets, *In: CBMSNSF Regional Conference Series in Applied Mathematics*, *SIAM*, Philadelphia, PA. Vol. 61.

Domingues, M. O., O. J. Mendes, and A. Mendes da Costa (2005), Wavelet techniques in atmospheric sciences, *Advances in Space Research*, *35*(5), 831–842.

Farge, M., K. Schneider, and N. Kevlahan (1999), Non-Gaussianity and coherent vortex simulation for two-dimensional turbulence using an adaptive orthogonal wavelet basis, *Physics of Fluids*, *11*(8), SYMPOSIUM PAPERS, 2187 (15 pages).

Frick, P., S. L. Baliunas, D. Galyagln, D. Sokoloff, and W. Soon (1997), Wavelet analysis of stellar chromospheric activity variations, *The Astrophysical Journal*, *483*(1), 426–434.

Frick, P., A. Grossmann, and P. Tchamitchian (1998), Wavelet analysis of signal with gaps, *Journal of Mathematical Physics*, *39*(8), 4091–4107.

Frick, P., R. Beck, E. M. Berkhuijsen, and I. Patrickeyev (2001), Scaling and correlation analysis of galactic images. *Monthly Notices of the Royal Astronomical Society*, *327*(4), 1145–1157.

Iyemori, T., M. Nose, D. Han, Y. Gao, M. Hashizume, N. Choosakul, H. Shinagawa, Y. Tanaka, M. Utsugi, A. Saito, H. McCreadie, Y. Odagi, and F. Yang (2005), Geomagnetic pulsations caused by the Sumatra earquake on December 26, 2004, *Geophysical Research Letters*, *32*(20), L20807.

Karinen, A., and K. Mursula (2005), A new reconstruction of the Dst index for 1932-2002, *Annales Geophysicae*, *23*, 475–485.

Kherani, E. A., P. Lognonné, H. Hébert, L. Rolland, E. Astafyeva, G. Occhipinti, P. Coïsson, D. Walwer, E. R. de Paula (2012), Modelling of the total electronic content and magnetic field anomalies generated by the 2011 Tohoku-Oki tsunami and associated acoustic-gravity waves, *Geophysical Journal International*, *191*(3), 1049–1066.

Klausner, V., M. O. Domingues, O. Mendes, and A. R. R. Papa (2013), Tsunami effects on the Z component of the geomagnetic field, *Journal of Atmospheric and Solar-Terrestrial Physics*, *92*, 124–136.

Larsen, J., and C. Cox (1966), Lunar and solar daily variation in the magnetotelluric field beneath the ocean. *Journal of Geophysical Research*, *71*(18), 4441–4445.

Lognonné, P., E. Clévédé, H. Kanamori (1998), Computation of seismograms and atmospheric oscillations by normal-mode summation for a spherical earth model with realistic atmosphere *Geophysical Journal International*, *135*(2), 388–406.

Mallat, S. (1991), Multiresolution approximations and wavelets orthonormal bases, *Transactions of American Mathematical Society*, *315*, 334–351.

Mallat, S. (1999), A Wavelet Tour of Signal Processing, *Academic Press*, *Elsevier Science*, *ISBN 9780080520834*.

Manoj, C., A. Kuvshinov, S. Maus, H. Luhr (2006), Ocean circulation generated magnetic signals. *Earth, Planets and Space*, *58*, 429–437.

Manoj, C., S. Maus, and A. Chulliat (2011), Observation of Magnetic Fields Generated by Tsunamis, *EOS, Transactions American Geophysical Union*, *92*(2), 13–14.

Mendes, O. J., M. O. Domingues, A. Mendes da Costa, and A. L. Clúa de Gonzalez (2005), Wavelet analysis applied to magnetograms: Singularity detections related to geomagnetic storms, *Journal of Atmospheric and Solar-Terrestrial Physics*, *67*(17–18), 1827–1836.

Mendes da Costa, A., M. O. Domingues, O. Mendes, and C. G. M. Brum (2011), Interplanetary medium condition effects in the south atlantic magnetic anomaly: A case study, *Journal of Atmospheric and Solar-Terrestrial Physics*, *73*(11–12), 1478–1491.

Nesme-Ribes, E., P. Frick, D. Sokoloff, V. Zakharov, J. C. Ribes, A. Vigouroux, and F. Laclare (1995), Wavelet analysis of the maunder minimum as recorded in solar diameter data. *Comptes rendus de l'Académie des sciences, série II, Mécanique, physique, chimie, astronomie*, *321*(12), 525–532.

Occhipinti, G., P. Lognonné, E. A. Kherani, and H. Hébert (2006), 3D Waveform modeling of ionospheric signature induced by the 2004 Sumatra tsunami. *Geophysical Research Letters*, *33*, L20104.

Occhipinti, G., P. Coisson, J. J. Makela, S. Allgeyer, A. Kherani, H. Hébert, and P. Lognonné (2011), Three-dimensional numerical modeling of tsunami-related internal gravity waves in the Hawaiian atmosphere. *Earth Planets Space*, *63*(7), 847–851.

Occhipinti, G., L. Rolland, P. Lognonné, and S. Watada (2013), From Sumatra 2004 to Tohoku-Oki 2011: The systematic GPS detection of the ionospheric signature induced by tsunamigenic earthquakes. *Journal of Geophysical Research: Space Physics*, *118*(6), 3626–3636.

Parkinson, W. D. (1983), Introduction to geomagnetism, *Scottish Academy Press*, *Edinburg and London.*

Pararas -Carayannis, G. (2010), The Earthquake and tsunami of 27 February 2010 in Chile - Evaluation of source mechanism and of near and far-field tsunami effects, *Science of tsunami hazards*, *29*(2), 96–126.

Paschmann, G., and P. W. Daly (1998), Analysis Methods for Multi-Spacecraft Data, *ISSI Scientific Reports Series*, ESA/ISSI, *1*, *ISBN 1608-280X*.

Peltier, W. R., and C. O. Hines (1976), On the possible detection of tsunamis by a monitoring of the ionosphere, *Journal of Geophysical Research*, *81*(12), 1995–2000.

Rolland, L., G. Occhipinti, P. Lognonné, and A. Loevenbruck (2010), Ionospheric gravity waves detected offshore Hawaii after tsunamis. *Geophysical Research Letters*, *37*(17), L17101.

Russell, C. T., and R. C. Elphic (1978), Initial ISEE magnetometer results: magnetopause observations, *Space Science Reviews*, *22*(6), 681–715.

Stephenson, D., and K. Bryan (1992), Large-scale electric and magnetic fields generated by the oceans, *Journal of Geophysical Research*, *97*(10), 15467–15480.

Sonnerup, B. U. O., and L. J. Jr Cahill (1967), Magnetopause Structure and Attitude from Explorer 12 Observations, *Journal of Geophysical Research*, *72*(1), 171–183.

Sonnerup, B. U. O. (1976), Magnetopause and boundary, *in Physics of Solar-Planetary Environments*, *American Geophysical Union*, ed. D.J. Williams, 541–557.

Tyler, R. H., J. M. Oberhuber, and T. B. Sanford (1999), The potential for using ocean generated electromagnetic fields to remotely sense ocean variability. *Physics and Chemistry of the Earth, Part A: Solid Earth and Geodesy*, *24*(4), 429–432.

Tyler, R. H., S. Maus, and H. Luhr (2003), Satellite observations of magnetic fields due to ocean tidal flow. *Science*, *299*, 239–241.

Tyler, R. H. (2005), A simple formula for estimating the magnetic fields generated by tsunami flow. *Geophysical Research Letters*, *32*, L09608, 4 pp.

Utada, H., H. Shimizu, T. Ogawa, T. Maeda, T. Furumura, T. Yamamoto, N. Yamazaki, Y. Yoshitake and S. Nagamachi (2011), Geomagnetic field changes in response to the 2011 off the Pacific Coast of Tohoku Earthquake and Tsunami, *Earth and Planetary Science Letters*, *311*(1–2), 11–27.

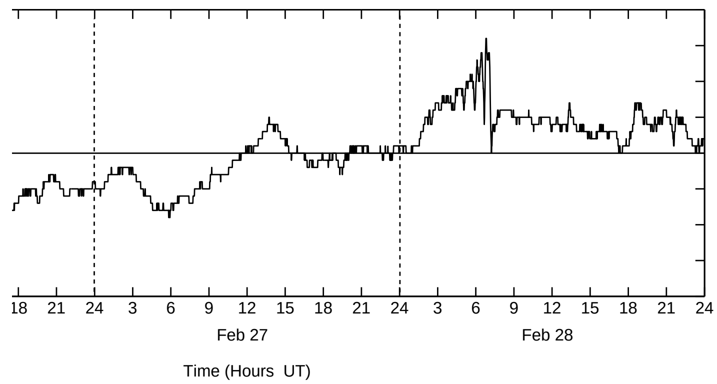

Figure 1. Minutely variation of the SYM-H index from the 26 to 28th of February, 2010. The vertical axis shows the provisional SYM-H signature and the horizontal axis shows the corresponding Universal time. The vertical dashed lines divide the tsunami event (February 27, 2010) from the previous day and the day after.

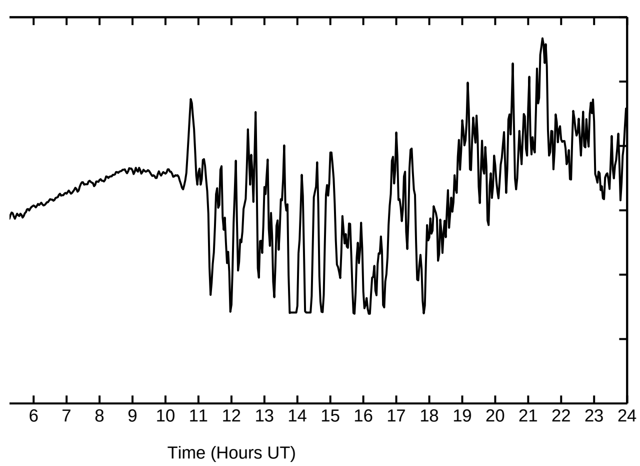

Figure 2. Variation of sea level at Callao La Punta, Peru, on the 27th of February, 2010.

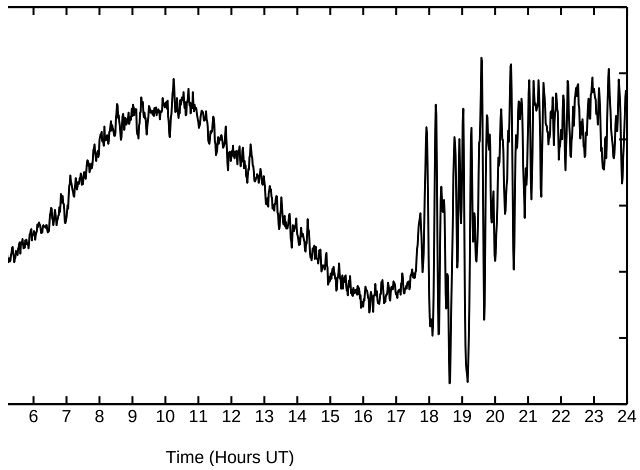

Figure 3. Variation of sea level at Papeete, French Polynesia, on the 27th of February, 2010.

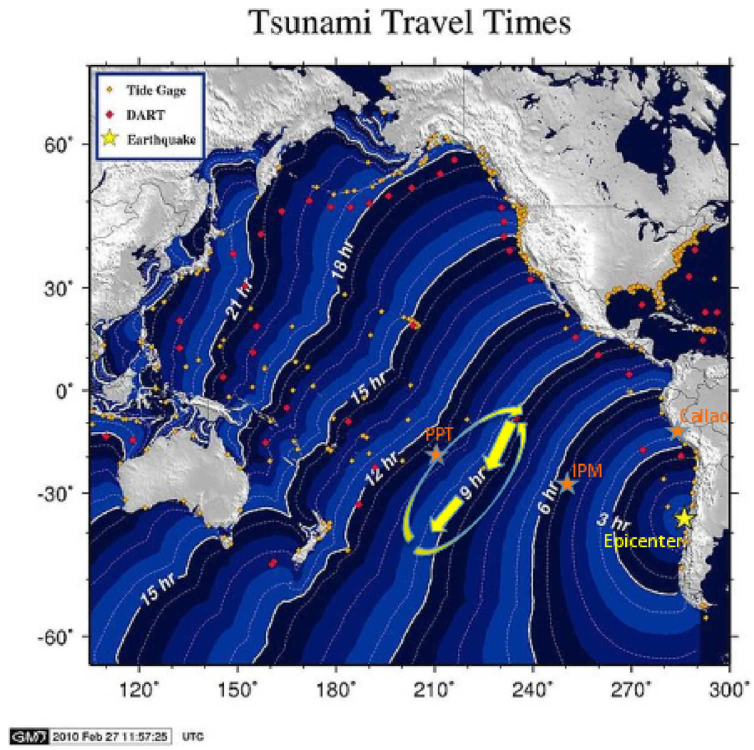

Figure 4. Adapted map of tsunami arrival times (courtesy of NOAA) showing the locations of Pt. Callao, and the PPT and IPM magnetic observatories. Also included is a diagrammatic example of tsunami-flow generated electric currents in the ocean: When the primary front has reached the 9-hr contour, motionally induced electric currents are generated in the sense of the straight yellow arrows. Because this induction is not uniform along the contour, and because electric charge must be conserved, electric currents such as shown by the curved arrows develop. Note that these electric currents (and the associated magnetic field) arrive in advance of the tsunami (see the animated tsunami simulation calculated with MOST forecast model provided on-line by the NOAA Center for Tsunami Research).

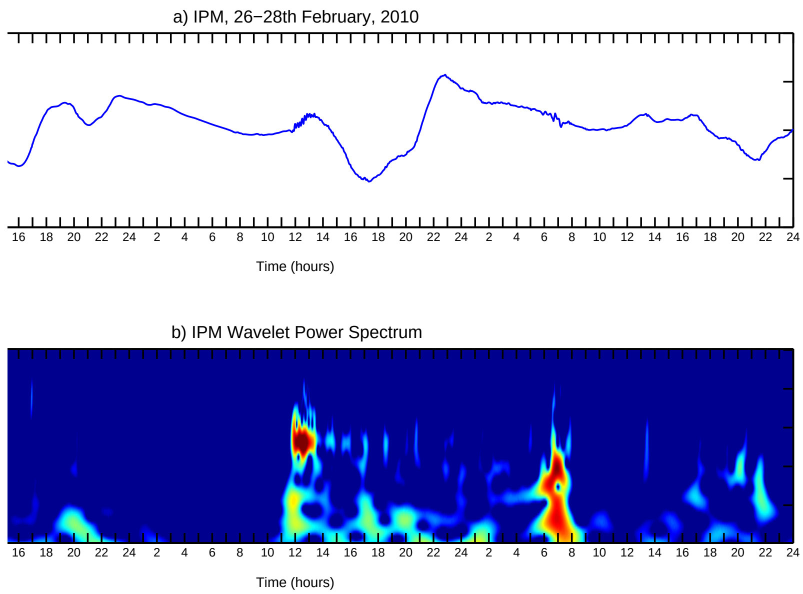

Figure 5. The GWT of IPM magnetograms for the days 26 to 28th of February, 2010. The top panel shows the filtered Z-component and the bottom panel presents the scalogram using Morlet wavelet, logarithmic scaled representing $\log 2(|W(a,b)|)$.

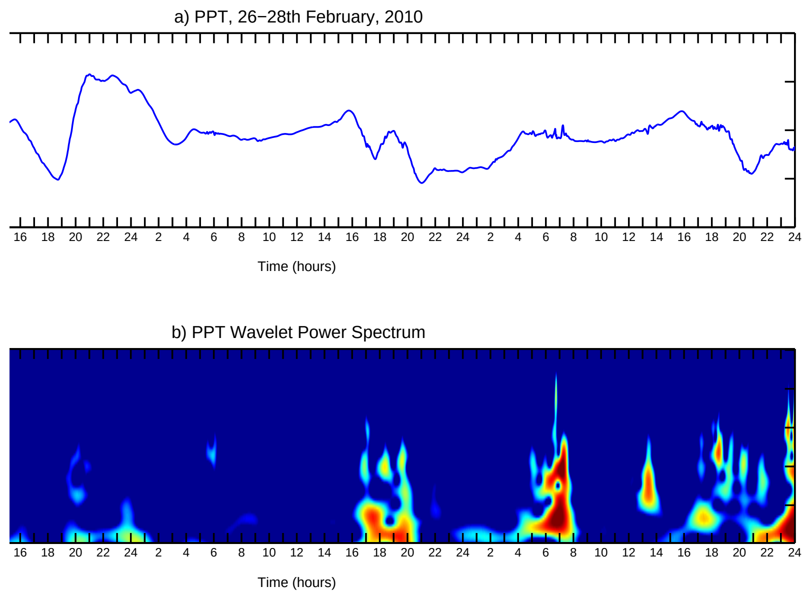

Figure 6. The GWT of PPT magnetograms for the days 26 to 28th of February, 2010. The top panel shows the filtered Z-component and the bottom panel presents the scalogram using Morlet wavelet, logarithmic scaled representing $\log 2(|W(a,b)|)$.

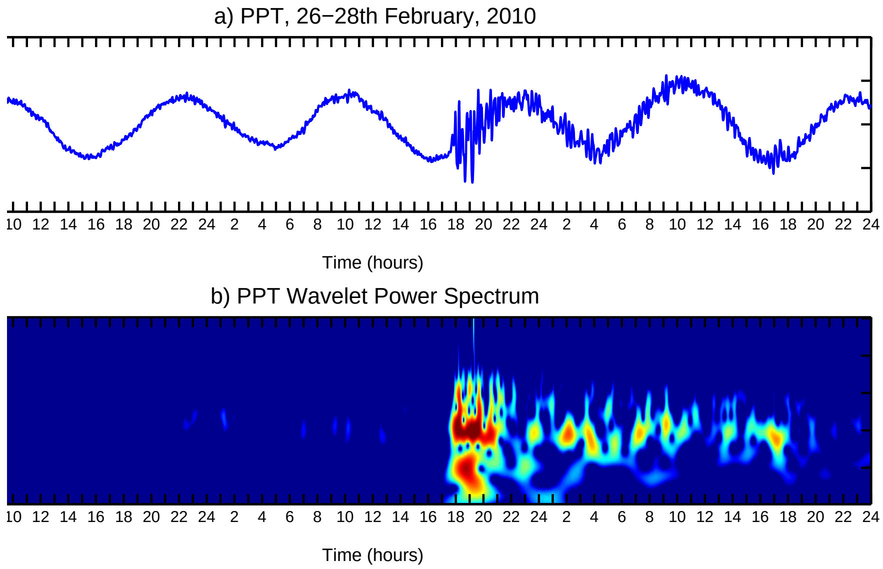

Figure 7. The GWT of PPT tide gauge dataset for the days 26 to 28th of February, 2010. The top panel shows the tide gauge data and the bottom panel presents the scalogram using Morlet wavelet, logarithmic scaled representing $\log 2(|W(a,b)|)$.

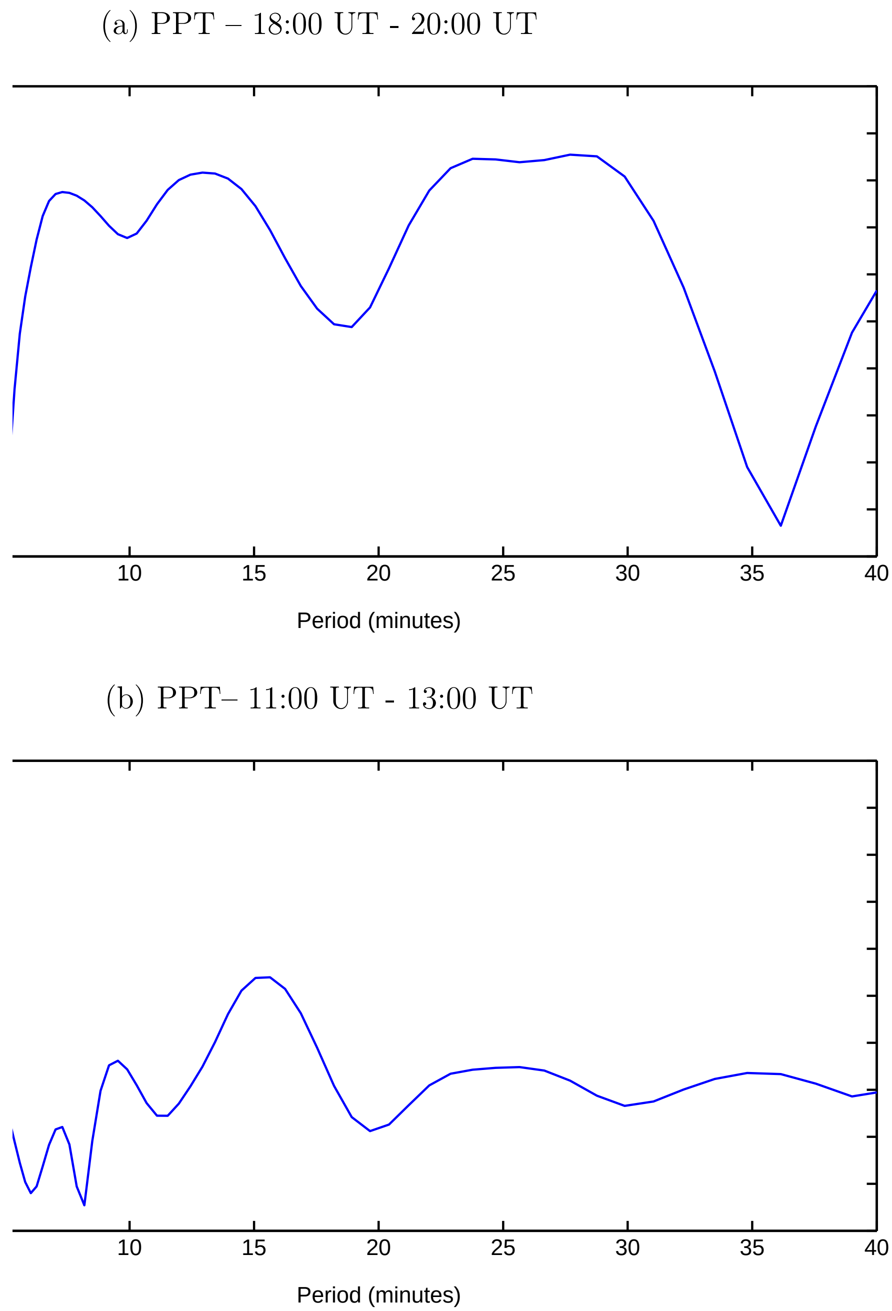

Figure 8. Modulus of the wavelet cross-correlation functions for PPT magnetogram and PPT tide gauge during the tsunami propagation (top panel) and the period before the tsunami arrival (bottom panel).

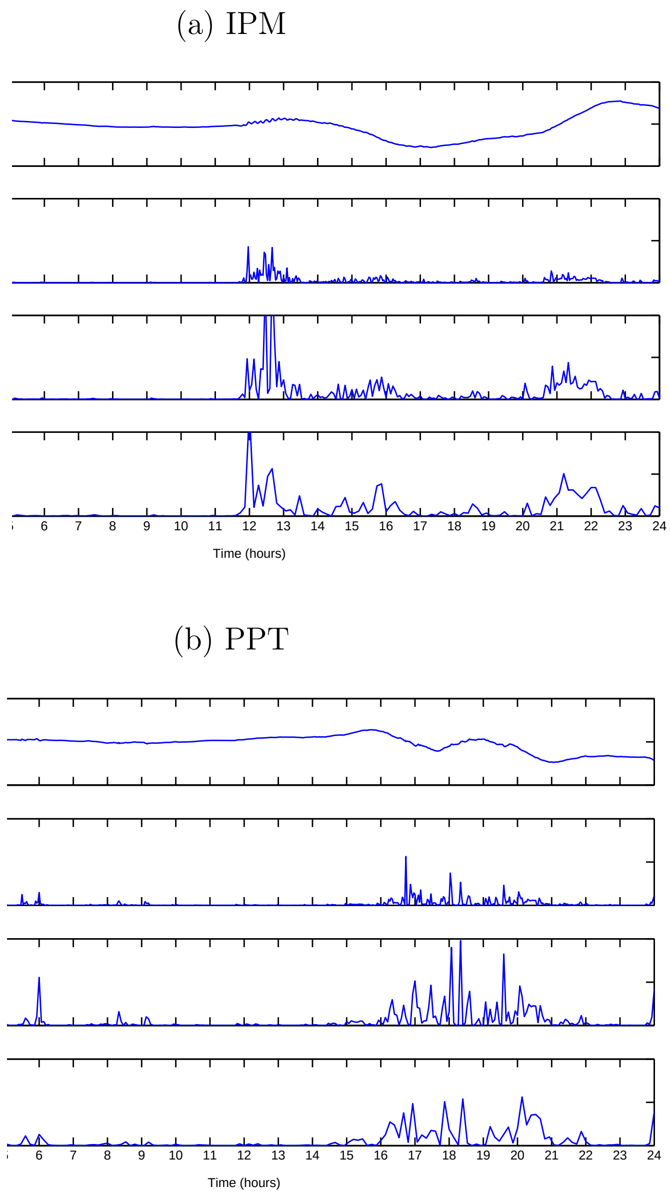

Figure 9. Magnetogram of the Z-component and the first three wavelet decomposition levels $dj = (d^j)^2$ where $j = 1, 2, 3$ with pseudo-periods of 2, 4 and 8 minutes, for IPM (a) and PPT (b), respectively.

(a) PPT - day before (b) PPT - day after

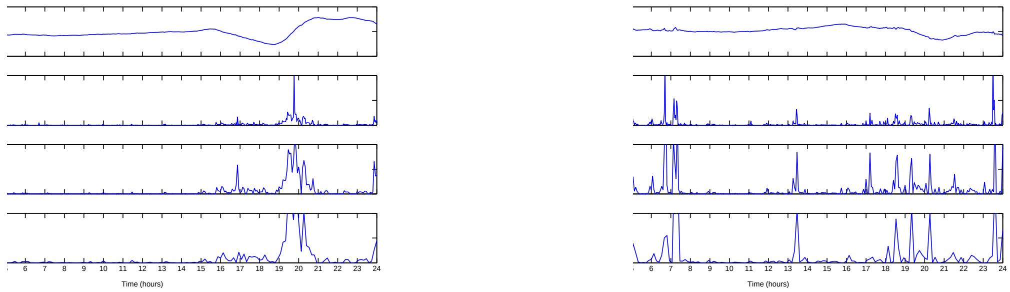

Figure 10. Magnetograms and the wavelet decomposition levels $dj = (d^j)^2$ for $j = 1, 2, 3$ for PPT: (a) for the day before of the tsunami arrival (26th February, 2010) and (b) the day after (28th February, 2010), respectively.

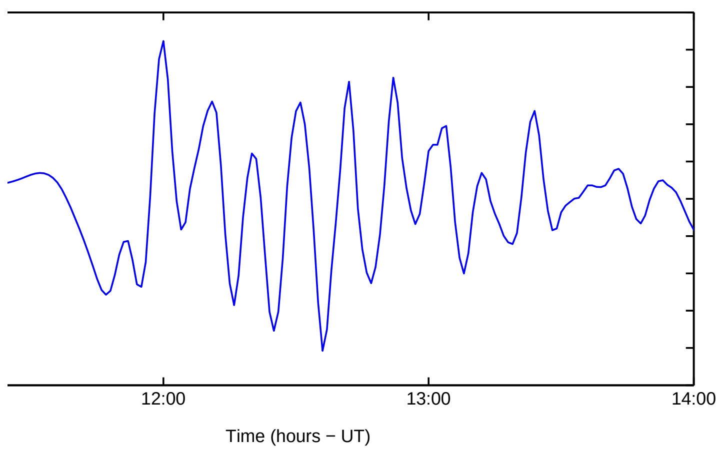

Figure 11. Variation of the filtered Z-component from 11:00 UT until 14:00 UT for IPM. Period of time corresponding to the tsunami propagation.

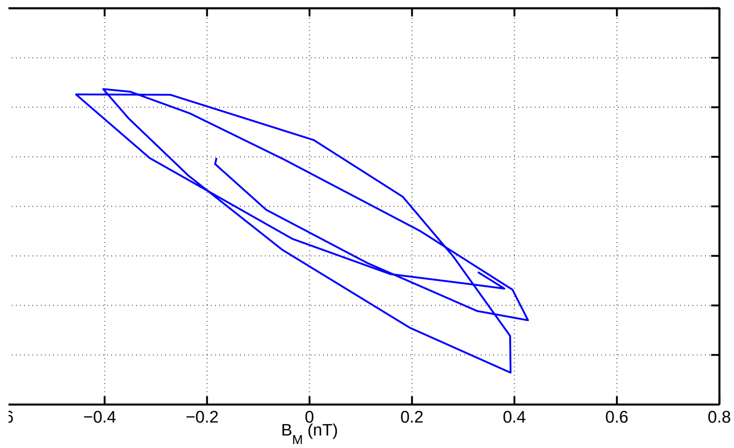

Figure 12. The transformation to the system of LMN coordinates for IPM on 27th February, 2010.

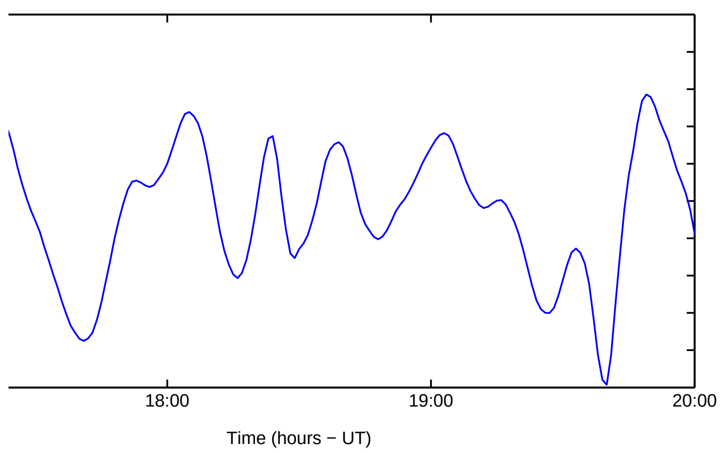

Figure 13. Variation of the filtered Z-component from 17:00 UT until 20:00 UT at PPT. Period of time corresponding to the tsunami propagation.

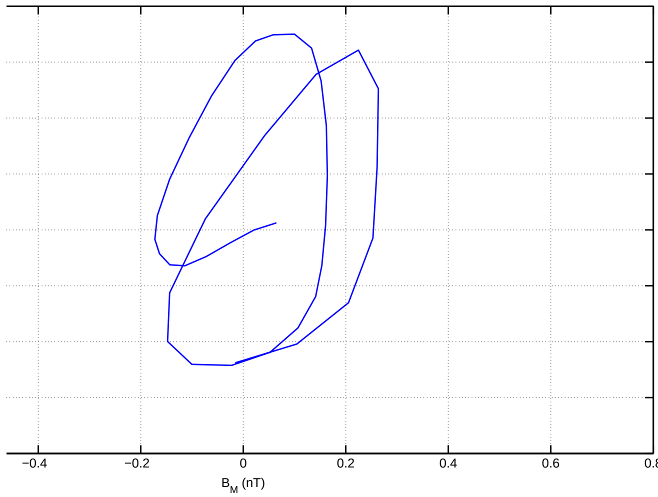

Figure 14. The transformation to the system of LMN coordinates for PPT on 27th February, 2010.

Table 1. INTERMAGNET network of geomagnetic observatories for the study of the Chilean tsunami, 2010.

Observatory	Geographic coord.		Geomagnetic coord.	
	Lat.($^\circ$)	Long.($^\circ$)	Lat.($^\circ$)	Long.($^\circ$)
IPM	-27.90	-109.25	-19.63	-34.47
PPT	-17.57	-149.58	-15.03	-74.53